Phys. Med. Biol. **42** (1997) 371–387. Printed in the UK PII: S0031-9155(97)71995-X

Single- and dual-energy CT with monochromatic synchrotron x-rays

F A Dilmanian†, X Y Wu†, E C Parsons†, B Ren†, J Kress†[+], T M Button‡, L D Chapman†[*], J A Coderre†, F Giron‡, D Greenberg†, D J Krus§, Z Liang‡, S Marcovici‖, M J Petersen‡, C T Roque‡, M Shleifer†, D N Slatkin†, W C Thomlinson†, K Yamamoto¶, and Z Zhong†

† Brookhaven National Laboratory, Upton, NY 11973-5000, USA
‡ State University of New York, Stony Brook, NY 11794, USA
§ Harshaw Crystal Products Group, Bicron, Solon, OH 44139, USA
‖ Analogic Corporation, Peabody, MA 01960, USA
¶ Hamamatsu Photonics K.K., Hamamatsu City, 431-32 Japan

Received 12 February 1996, in final form 11 November 1996

Abstract. We explored the potential for clinical research of computed tomography (CT) with monochromatic x-rays using the preclinical multiple energy computed tomography (MECT) system at the National Synchrotron Light Source. MECT has a fixed, horizontal fan beam with a subject apparatus rotating about a vertical axis; it will be used for imaging the human head and neck. Two $CdWO_4$-photodiode array detectors with different spatial resolutions were used. A 10.5 cm diameter acrylic phantom was imaged with MECT at 43 keV and with a conventional CT (CCT) at 80 kVp: spatial resolution $\approx$ 6.5 line pairs (lp)/cm for both; slice height, 2.6 mm for MECT against 3.0 mm for CCT; surface dose, 3.1 cGy for MECT against 2.0 cGy for CCT. The resultant image noise was 1.5 HU for MECT against 3 HU for CCT. Computer simulations of the same images with more precisely matched spatial resolution, slice height and dose indicated an image–noise ratio of 1.4:1.0 for CCT against MECT. A 13.5 cm diameter acrylic phantom imaged with MECT at $\approx$ 0.1 keV above the iodine K edge and with CCT showed, for a 240 μg I ml^{-1} solution, an image contrast of 26 HU for MECT and 13 and 9 HU for the 80 and 100 kVp CCT, respectively. The corresponding numbers from computer simulation of the same images were 26, 12, and 9 HU, respectively. MECT's potential for use in clinical research is discussed.

1. Introduction

Refinements of computed tomography (CT), such as improvements in the source, detector, gantry, data acquisition, system control, image processing, image corrections and display, have broadened CT's clinical usefulness (Hamberg *et al* 1994). In particular, dynamic focal spot technique, dual-slice scanning, and high-resolution CT (Arenson 1995), helical or spiral CT (Kalender 1995), CT angiography (Rubin *et al* 1993), and ultrafast CT (McCollough 1995) have been introduced. Nevertheless, limitations from the large beam-energy width have not been overcome, and all current CT systems employ bremsstrahlung radiation, which inherently has a broad energy spectrum. Development of high-intensity synchrotron

[+] Present address: Physics Department, University of Würzburg, Würzburg, Germany.
[*] Present address: Center for Synchrotron Radiation Research and Instrumentation, Illinois Institute of Technology, Chicago, IL 60616, USA.

0031-9155/97/020371+17$19.50

x-ray beamlines in the last decade allowed advances to be made in monochromatic CT (Thompson *et al* 1984, Dilmanian *et al* 1991, Dilmanian 1992, Nachaliel *et al* 1992, Takeda *et al* 1994, Kress 1995, Wu *et al* 1995), which further improved CT's soft-tissue contrast, image quantification, and elemental sensitivity.

This paper characterizes multiple-energy computed tomography (MECT), a monochromatic CT system under development at the X17B superconducting wiggler beam line of the National Synchrotron Light Source, Brookhaven National Laboratory (BNL). Single- and dual-energy images from the preclinical MECT system are presented, together with conventional CT (CCT) images of the same subjects under similar conditions. Computer simulations of both MECT and CCT results are also reported.

Upon its completion, the MECT system will first be applied to certain clinical studies in neurology and cardiology. The system will have an $\approx$ 19.5 cm field of view (FOV) for symmetric, and $\approx$ 36 cm useful FOV for asymmetric scanning (i.e., when the beam covers the rotation axis and only one half of the subject). The patient's chair will rotate at $72^\circ\ s^{-1}$. Clinical research with MECT is mainly expected to involve high-sensitivity and/or high-resolution, quantitative CT angiography in conjunction with I or Gd contrast agents using helical CT at a single breathhold. It will also encompass dual-energy quantitative CT (DEQCT) (see, for example, Cann and Genant 1980, Goodsitt *et al* 1994) primarily for assessing the evolution of carotid artery plaques through their evolutionary stages: lipidosis, fibrosis, and calcification (Seeger *et al* 1995). Emphasis will be on longitudinal studies in individual patients. We expect that MECT's reduced image noise and enhanced tissue contrast compared with CCT will not only allow better tissue characterization, but also reduce the number of patients required to attain a given statistical significance of results. Applications of MECT to other diagnostic and prognostic problems, including early detection of neurological disorders, can only be assessed by clinical research. Conceivably, MECT may also be used to image lesions of the thorax and the abdomen.

In its current state, MECT is synchrotron based; thus, its use is limited to a few research programmes in large laboratories. However, sufficient clinical incentive may be developed at the NSLS medical beamline to justify the commercial development of compact, non-synchrotron-based clinical monochromatic CT systems.

2. Advantages of monochromatic CT

In the following discussion, the same subject absorbed dose was assumed for the monochromatic and the polychromatic methods.

(i) Monochromatic beams eliminate beam-hardening artifacts (Stonestrom *et al* 1981), thus improving the detectability of low-contrast lesions and image quantification.

(ii) Monochromatic beams allow the beam's energy to be optimized for a patient's size (Grodzins 1983a, Spanne 1989). Although the optimal energies depend on whether or not contrast is sought for lesions of different mean atomic number or different densities, in both cases the optimal energy is defined within $\approx$ 10 keV for human studies. On the other hand, CCT's energy spectra are typically 60–90 keV wide (40–60 keV full-width at half-maximum). For example, a 120 kVp beam, filtered with 2.5 mm Al and 0.12 mm Cu, extends (at one-tenth of maximum) from 25 to 115 keV with a mean energy of $\approx$ 60 keV. The lower end of the spectrum adds radiation dose but makes little contribution to image quality because of its low transmission through the subject, while the higher end produces little soft-tissue contrast.

(iii) In contrast imaging, a monochromatic beam allows the beam's energy to be tuned

immediately above the K edge of the contrast element (Grodzins 1983b) (K-edge imaging, hereafter), thus maximizing the signal's size. For iodine (a K edge of 33.17 keV) the resulting gain in image contrast can be threefold or more, depending on the polychromatic beam spectrum (iodine's attenuation coefficient rises $\approx$ 5.6-fold at the K edge). Furthermore, images can be acquired immediately above and below the K edge and then logarithmically subtracted to improve the contrast agent's quantification. The latter method is referred to as K-edge subtraction, and is undergoing clinical evaluation at several synchrotron beamlines for transvenous coronary angiography (see, for example, Rubenstein *et al* 1986). Although implementation of monochromatic CT at the iodine K edge is suboptimal for head imaging and impractical for chest/abdomen imaging because of the low transmission of the 33 keV x-rays in tissue (transmissions of 33 and 50 keV x-rays through 40 cm soft tissue, i.e. the depth of the human adult shoulder musculature, are 1/292 000 and 1/7300, respectively), it can readily be used for imaging the human neck. On the other hand, limitations of a 33 keV beam for whole-body CT and the prospects for developing a clinical narrow-energy-band CT may encourage the evolution of CT contrast agents with higher-Z elements than iodine, such as gadolinium (K edge = 50.23 keV) (see Zeman and Siddons 1990).

(iv) The well defined energy of the monochromatic beam would make it ideal for DEQCT. The method, which is in effect dual-photon absorptiometry in the CT mode, produces two separate images of light- and intermediate-Z elements.

3. MECT system design

3.1. Beam and monochromator

The X17B beamline is the central, 5 mrad sector of the X17 beamline at the NSLS's 2.52 GeV x-ray storage ring (van Steenbergen *et al* 1980). The X17 wiggler was operated at 4.66 T during our experiments to provide a 19.8 keV beam critical energy, E_c (E_c is the energy that demarcates the spectrum into halves, each with equal power). Filters between the wiggler source and the 22.3 m distal monochromator are (i) 0.39 mm of graphite, (ii) three Be windows totalling 1.27 mm, and (iii) a 3 mm Si filter, positioned immediately upstream from the monochromator and halving the heat loading on the crystal. A fourth filter, called a 'bowtie' beam filter (Joseph 1981), was used only for some of the images. Its purpose is to preferentially reduce the peripheral beam intensity, and so to improve the uniformity of the subject's absorbed dose across the slice and protect the outermost detector elements from excessive dose. Our bowtie filter consisted of a 175 mm thick acrylic plate with a cylindrical opening of 170 mm diameter in its centre; it was positioned 35.5 m from the source. The typical beam lifetime is 35 h; the maximum and minimum ring currents during the experiments were about 250 and 110 mA.

The experiments reported in this paper were carried out in the two X17B experimental areas located in series: the Materials Science area, X17B1 (closer to the source, used for the first experiments) and the Synchrotron Medical Research Facility (SMERF; Thomlinson *et al* 1988), X17B2. Table 1 lists experimental parameters used in these two areas.

The monochromator is a tunable, fixed-exit two-crystal Laue–Laue device, producing a monochromatic beam parallel to the incident white beam with a vertical offset of 15 mm (Shleifer *et al* 1994). It employs two flat Si $\langle 111 \rangle$ crystals, 1 mm thick each, mounted on independent joystick (gimbals) mechanisms. Its energy range was 24.5–51.2 keV. Table 2 summarizes the parameters of the monochromatic beams at 33.2 and 43 keV. The monochromator was 'detuned' in our experiments, i.e. the second crystal was aligned slightly nonparallel to suppress beam harmonics; this reduced the beam's intensity to only

Table 1. The beam in the B1 and B2 areas.

Beamline	Source-to-subject distance (m)	Source to vacuum-exit port distance (m)	Total Be windows (mm)	Bowtie filter
X17B1	29	27	1.27	No
X17B2	39	32.5	2.54	Yes

Table 2. Monochromatic beam parameters.

Beam energy (keV)	Monochromator's integrated reflectivity (eV)	Energy spread at 2.5 mm slice height (eV)	3rd harmonic yield w/tuned monochromator (%)	3rd harmonic at 20% of the tuned beam (%)	Calc. B2 flux at 20% detuning (photons s^{-1} mm^{-2})
33.2	1.1	35	1	0.02	8.8×10^7
43	1.55	58	0.1	< 0.002	1.3×10^8

Table 3. Structural parameters of the detectors.

Parameters	High-resolution detector	Low-resolution detector
Centre-to-centre element spacing (mm)	0.5	1.844
Active element width (mm)	0.4	1.5
Element height (mm)	6.0	28.0
Scintillator thickness (mm)	3.5	2.4
Number of elements per module	32	16
Detector masking (mm)	None	0.922

13–25% of the monochromator's peak yield, while reducing the beam harmonics to below 0.02%.

3.2. Detectors

Two different modular $CdWO_4$-photodiode linear array detectors were used; both employed PIN (p-type intrinsic n-type) diodes. One (the high-resolution detector) was used for some of the images described below; however, it later exhibited excessive nonlinearity. The other (the low-resolution detector) was borrowed from the Analogic Corp. (Peabody, MA). Their structures are summarized in table 3.

3.3. The data-acquisition system

The front-end data-acquisition system (DAS) was developed by Analogic Corp. with a readout dynamic range of 10^6:1. It was connected to a DEC Alpha 400 model 3000 through a custom-designed interface board fabricated by Wu and his colleagues at BNL via a direct-memory access (DMA) board on Alpha's turbochannel bus. Data were transferred from the computer's memory to a high-speed disk, using a pair of buffer memories at each step to allow uninterrupted data collection. The interface allowed a maximum sustained data flow rate of 2 Mbyte s^{-1}; the duration was limited only by the disk's storage capacity, 1 Gbyte.

3.4. The image reconstruction program

The image reconstruction program developed by Wu at BNL used the filtered backprojection method; filtration is carried out in Fourier space and the backprojection is executed in configuration space. The program allows the isocentre of the rotating subject to be anywhere with respect to the detector, so simplifying alignment of the MECT system.

4. The CCT system

A GE HiSpeed CT scanner (General Electric Medical Imaging Systems, Milwaukee, WI) at the Department of Radiology, Health Sciences Center, State University of New York at Stony Brook, was used as the CCT to compare CCT and MECT images. The half-value layer (HVL) for the 80 and 100 kVp energy settings used in our studies were 4.2 and 5.7 mm Al, respectively. These HVLs were used in our computer simulations to estimate the thickness of filters in the beam, which allowed us to deduce that the mean energies of the 80 and 100 kVp beams were 43 and 55 keV, respectively.

5. Computer simulations

Computer simulations were performed for all the phantom images. The program simulates circular phantoms. It does not trace individual photons. Instead, it calculates, for a single beam energy at a time, the number of photons entering and exiting the phantom along each detection path, and broadens the exit number by a normally distributed noise, which is justified because of the large number of photons in the beam. X-ray beams are followed from the source to the individual detector elements. The detector and the DAS noise are assumed to be negligible compared to the photon noise, and are not included. In the polychromatic beam, photons are grouped in 1 keV bins; they are treated like monochromatic photons within each bin. The detected signal is the sum of the photons detected from individual bins multiplied by the bin's energy (assuming that the detector has a perfect sensitivity for all energies). Identical image-reconstruction parameters were used for both the simulations and the experiment.

6. Experimental methods

6.1. General

Data were collected at the rate of 1440 projections s^{-1}. During the off-line image analysis, 24 such projections were averaged to form one projection for reconstruction. The rotation speed of the subject's apparatus was only $24^\circ\ s^{-1}$ because of the monochromator's relatively low output. The monochromator's detuning was varied within 13–25% of the beam's peak yield to keep the detector's signal constant as the synchrotron's current decayed. Two separate 360° data were collected with one lateral translation of the subject's rotation axis corresponding to one-half of one inter-element detector spacing between collections. Most of the images presented were interlaced during the reconstructions (Dilmanian 1992, Kress 1995). Reference data (i.e., data taken with no subject in the beam), collected before and after each subject slice was scanned, were used to calculate the absolute transmission. Frequent collection of reference data minimized variations in the beam profile's shape that were attributable to instabilities in the monochromator. Nevertheless, uncorrected instabilities, which amounted to $\approx 0.2\%$ peak-to-peak for the typical 60 s elapse between

consecutive air measurements, were the main limitation of the present system's image quality. These instabilities decreased with increasing monochromator detuning. The detection system's dark current was measured once every few hours. Short-term oscillations of the beam's intensity, which occurred with a constant beam profile, were compensated for by using data from the two unattenuated ends of the fan beam, designated 'air channels'. Linear variations of the beam profile's shape were corrected by linear interpolation between these ends (Kress 1995). The detector's nonlinearities were uncorrected in the images presented. In some of the phantom images shown, ring artifacts were removed by software. The ring-removal routine detected derivatives in the radial direction, centred at the scanning isocentre. Certain thresholds were set to identify the rings, normally within a few CT numbers. The signal from the ring was then scaled by a common factor, after which the average ring value matched the interpolation of the average values of its neighbours.

Table 4. Main parameters of the MECT measurements.

							MTF	
Subject no	Subject	X17 area	Bowtie filter	Detector	Beam energy (keV)	Image interlacing	Curve	10% cutoff frequency (1p cm^{-1})
1	Rabbit lower head	B1	out	high res.	43	yes	figure 2(d)	12.2
2	Ring phantom	B1	out	high res.	43	yes	figure 2(d)	12.2
3a	Low-contrast phantom	B1	out	high res.	43	no	figure 2(c)	7.0
3b	Low-contrast phantom	B2	in	low res.	43	yes	figure 2(a)	4.9
4a	Iodine phantom	B2	in	low res.	43	yes	figure 2(a)	4.9
4b	Iodine phantom	B2	in	low res.	≈ 33.25 ≈ 33.09	yes	figure 2(a)	4.9

6.2. Individual experiments

Table 4 summarizes the main parameters for the experiments reported. The MECT slice heights were 1.9 and 2.6 mm FWHM for experiments in the B1 and B2 rooms, respectively; figure 1 shows the B2 beam profile, measured close to the detector. The slice height was 3.0 mm for all CCT images. The pixel size was 0.445 mm for MECT with the high-resolution detector, and 0.488 mm for CCT. The spatial resolutions shown are the frequency at 10% cutoff value of the modulation transfer function (MTF). The MTFs were measured with a standard 'impulse' phantom, i.e. a phantom including a thin, vertical axial metal wire (Gammex RMI, Middleton, WI). The profile of the image of the wire was first fitted with a Gaussian function, and then analysed to generate the MTF (Nickolloff and Riley 1985). Figure 2 shows the MTF curves for the images presented.

The individual subjects' studies are described below. The experimental details and the results are summarized in tables 4 and 5, and the simulation results are also given in table 5. The image noise was measured as a standard deviation of the CT numbers inside a region of interest (ROI). The ROIs for individual phantom channels were concentric circles of $\approx 2/3$ of its diameter. Dosimetry for both MECT and CCT measurements were carried out with TLDs.

6.2.1. Subject 1: a rabbit's lower head. As a qualitative experiment, an anesthetized rabbit was imaged in the B1 room at the level of the cerebellum (figure 3). The slice diameter

Table 5. A summary of results: MECT, CCT and simulations (see table 4 for other experimental details).

Experiment No and beam	Detector imaging mode	Surf. dose (cGy)	Slice height (mm)	Spatial resol. (lp cm^{-1})	Image noise		Recon. filter, cutoff	Image contrast at 240 μg I ml^{-1}	
					Exp. (HU)	Sim. (HU)		Exp.(HU)	Sim. (HU)
Low-contrast phantom									
MECT 3a, 43 keV	High res. w/o interlac.	3.1	1.9	7	≈ 1.5	1.5	Hanning, 0.5	—	—
MECT 3b, 43 keV	Low res. w/interlac.	3.4	2.6	4.9	≈ 1	1.1	Hanning, 0.6	—	—
CCT, 80 kVp, 400 mA s	—	2.0	3.0	6.5	≈ 3	2.1	Standard	—	—
Iodine phantom									
MECT 4a, 43 keV	Low res. w/interlac.	2.5	2.6	4.9	≈ 1	2.3	Hanning, 0.5	18	17
MECT 4b, 33.25 keV	Low res. w/interlac.	4.4	2.6	4.9	≈ 3	1.5	Hanning, 0.5	26	26
CCT, 80 kVp, 800 mA s	—	2.8	3.0	6.5	≈ 3	2.6	Standard	13	12
CCT, 100 kVp, 400 mA s	—	2.4	3.0	6.5	≈ 3	1.9	Standard	9	9

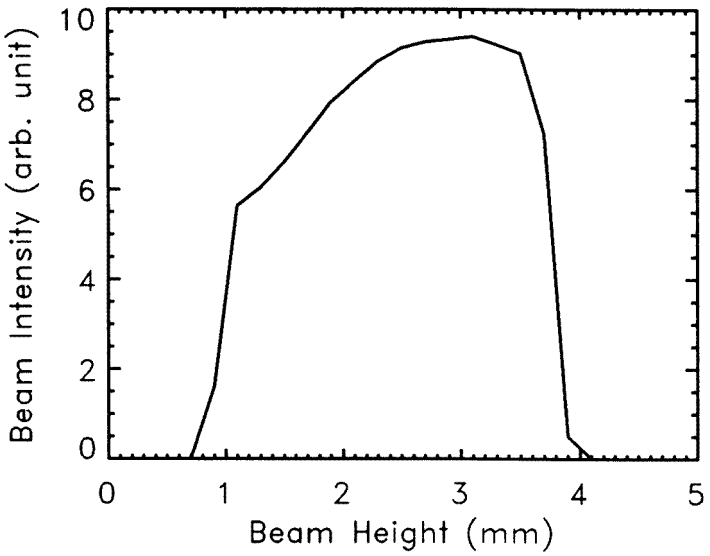

Figure 1. The vertical profile of the monochromatic beam.

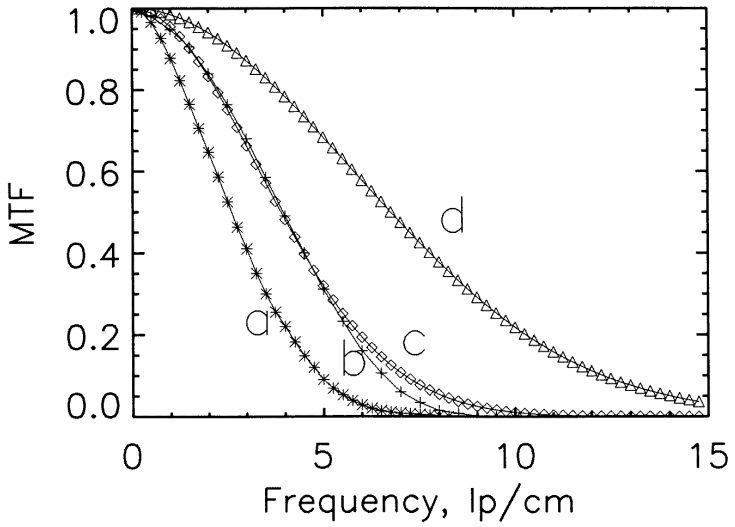

Figure 2. MTF curves (see also table 4): (a) MECT, B2 room, low-resolution detector, images interlaced, 10% cutoff at 4.9 lp cm^{-1}; (b) CCT with standard reconstruction filter, 10% cutoff at 6.5 lp cm^{-1}; (c) MECT, B1 room, high-resolution detector, images not interlaced, 10% cutoff at 7.0 lp cm^{-1}; (d) MECT, B1 room, high-resolution detector, images interlaced, 10% cutoff at 12.2 lp cm^{-1}.

was $\approx$ 10.5 cm, and the skin absorbed dose was $\approx$ 6 cGy. The image was reconstructed with a Hanning filter with a cutoff at 60% of the Nyquist frequency; the two images were interlaced, as described above. A similar slice was imaged with CCT (figure 4) at a 3 mm slice height, 80 kVp and 800 mA s; the skin dose was $\approx$ 4 cGy. The product of dose and exposed area (MECT, 1.9 mm slice height; CCT, 3 mm) was the same for the two images.

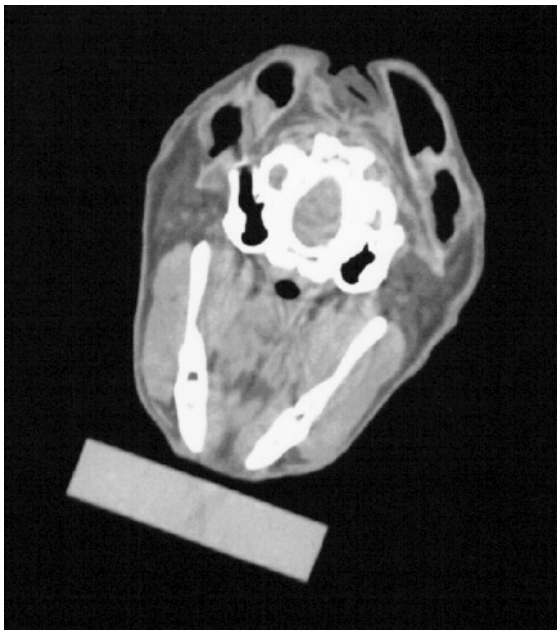

Figure 3. An MECT image of a rabbit's lower head at 43 keV and 6 cGy.

Figure 4. CCT of the rabbit's neck at 80 kVp and 800 mA s.

Both images delineate the muscle (lighter regions) from the subcutaneous fat. The dark bands along the continuation of the two jaw lines in the CCT image, which are absent from

the MECT image, are assumed to be beam-hardening artifacts. To confirm this, the rabbit was also imaged at 1 mm slice height (not shown); the dark bands persisted.

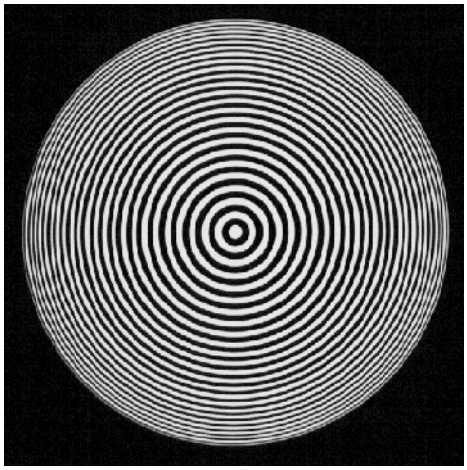

Figure 5. A 43 keV MECT image of the ring phantom.

6.2.2. Subject 2: the ring phantom. The phantom was a 98 mm diameter acrylic cylinder with concentric, circular 4 mm deep air grooves in its upper surface. The grooves had equal wall and valley thicknesses that decreased with increasing radius, from a 1.5 mm wide inner groove 2.3 mm from the cylinder axis to a 0.3 mm wide outer groove 48.5 mm from the axis. Figure 5 shows a 43 keV MECT image of the phantom, obtained at a surface dose was $\approx$ 7 cGy. The reconstruction used a ramp filter with a cutoff frequency equal to the Nyquist frequency; the images were interlaced. The MTF's 10% cutoff was 12.2 lp cm^{-1}; the high resolution of the image is indictated by the visibility of the 0.3 mm wide outermost groove. This phantom was not imaged by CCT.

6.2.3. Subject 3: the low-contrast standard phantom. The phantom was a 10.5 cm diameter acrylic cylinder that includes two conical inserts of the Gammex RMI (Middleton, WI) standard CT phantom inserts. One of these was the low-contrast insert (part No 460-013A) with five cylindrical, paraxial 0.6% contrast rods of 8.0, 5.6, 4.0, 2.8, and 2.0 mm diameters; the second one was the plain insert (part No 460-010). The phantom was imaged at 43 keV, once in the B1 and once in the B2 room.

Measurement a: B1 room. The phantom was imaged in the B1 room with the high-resolution detector, without interlacing, and at 3.1 cGy surface dose (figure 6(a)).

Measurement b: B2 room. The phantom was imaged in the B2 room with the low-resolution detector, with interlacing, and at 2.6 cGy surface dose (figure 6(b), left-hand side).

CCT measurement. The phantom was imaged at 80 kVp and 400 mA s, at 3 mm slice height, and 3.0 cGy surface dose (figure 6(c), left-hand side).

The B1 measurement and the CCT measurement are nearly matched in their parameters: the B1 image has 7 lp cm^{-1} spatial resolution while CCT has 6.5 lp cm^{-1}; the B1 image has 0.445 mm pixel size, CCT has 0.488, and in both the dose multiplied by the slice height

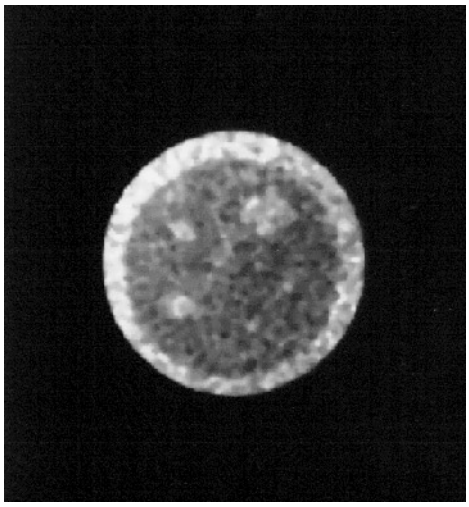

(a)

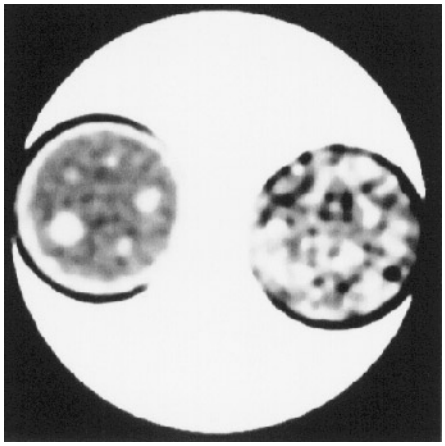

(b)

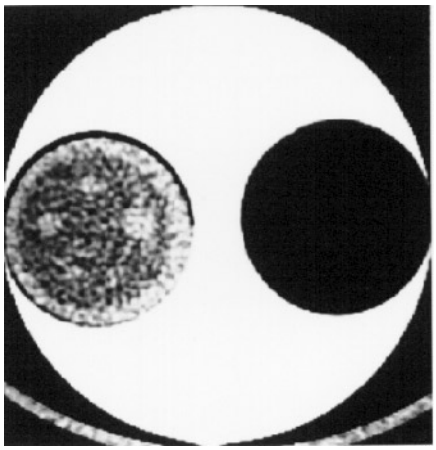

(c)

Figure 6. (a) An X17B1 MECT image of the low-contrast phantom. (b) An X17B2 MECT image of the low-contrast phantom. (c) A CCT image of the low-contrast phantom.

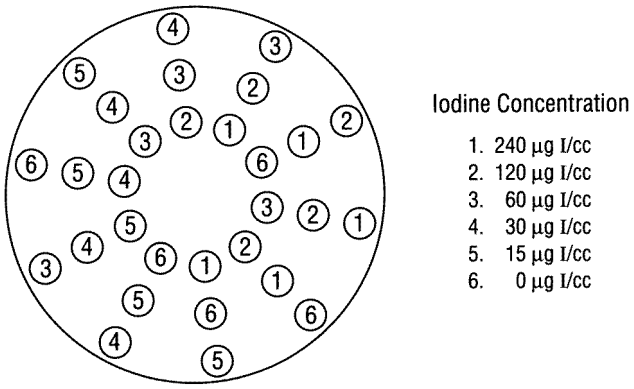

Figure 7. The pattern of the solutions in the iodine phantom.

was 6.0 cGy mm. However, the image noise was $\approx$ 1.5 HU for the B1 image and $\approx$ 3 HU for the CCT image. All five inserts are detected in the B2 image, compared to four or five in the B1 image (where the phantom's body and the plain insert are not visible), and four or five in the CCT image.

Our computer simulations were used to reproduce the B1 and the CCT images described above. The same pixel size (0.445 mm) and the same MTF curves (with 7 lp cm^{-1} 10% cutoff) were assumed. The results were 1.5 HU for the B1, and 2.1 HU for the CCT (see table 5), indicating a 1.4:1.0 ratio between the noise values for these two images.

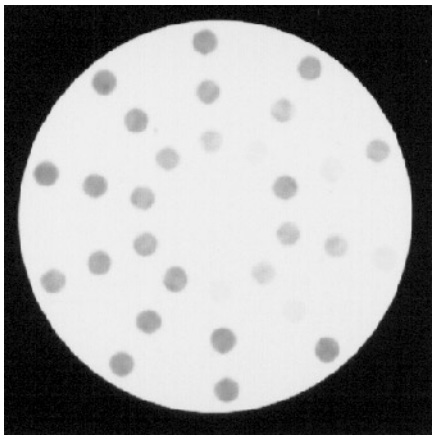

Figure 8. The iodine phantom imaged by MECT at 43 keV.

6.2.4. Subject 4: iodine phantom. The phantom was a 135 mm diameter, 3 cm long acrylic cylinder containing 30 11 mm diameter paraxial cylindrical channels. The channels were arranged in five diametric arrays of six channels each, positioned 36 apart. Figure 7 shows the pattern of the channels, and the channels' iodine concentrations. This design allowed individual iodine concentrations to be imaged at three different distances from the phantom's centre and to be averaged, thus minimizing possible radial effects in the image.

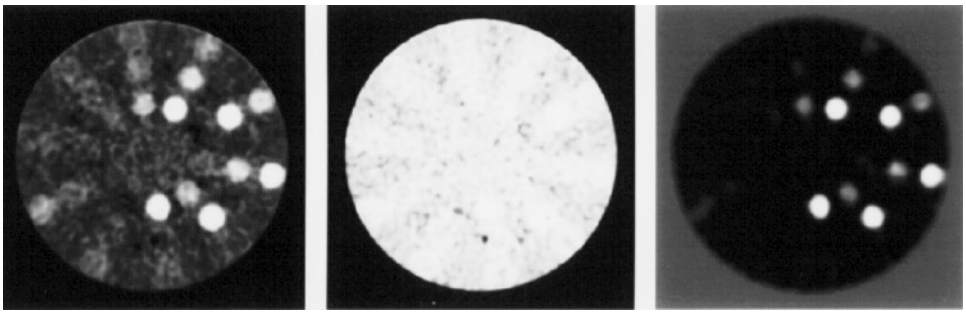

Figure 9. The iodine phantom imaged (from the left) above the K edge, below, and subtracted.

Measurement a: 43 keV. The phantom was imaged by MECT at 43 keV, with image interlacing, at 2.5 cGy surface dose (figure 8).

Measurement b: iodine K-edge subtraction. The phantom was imaged, with interlacing, at beam energies of ≈ 33.25 keV and ≈ 33.09 keV, bracketing the iodine K edge.

The surface dose for each of the above- and below-the-edge images was 4.4 cGy. The results are shown in figure 9 (left, above the edge; centre, below the edge; right, the subtracted image). The latter, which gave the iodine density ρ_I in units of grams per millilitre, was obtained from the following equations:

$$\mu(1) = \mu_{m,water}(1)\rho_{water} + \mu_{m,I}(1)\rho_I$$
$$\mu(2) = \mu_{m,water}(2)\rho_{water} + \mu_{m,I}(2)\rho_I.$$

Here, the indices 1 and 2 indicate 33.09 and 33.25 keV energies, and $\mu(1)$ and $\mu(2)$ are the linear attenuation coefficients of the iodine channel in the two images of different energies. Substituting the mass attenuation coefficients $\mu_{m,water}(1)$, $\mu_{m,I}(1)$, $\mu_{m,water}(2)$, and $\mu_{m,I}(2)$ with 0.3246, 6.5417, 0.3227, and 35.6143 cm^2 g^{-1}, respectively, we obtain the following equation for ρ_I:

$$\rho_I = 0.0342[1.0058\mu(2) - \mu(1)]. \tag{1}$$

The measured values of $\mu(1)$, $\mu(2)$, and ρ_I are within 2% of the nominal values of the iodine attenuation coefficients and iodine solution concentrations, respectively; this is also within the precision of the compositions of our solutions.

CCT measurements. Two CCT measurements were made: (a) 80 kVp and 800 mA s, that is 2.8 cGy surface dose (not shown) and (b) 100 kVp and 400 mA s, 2.4 cGy (figure 10).

Figure 11 plots the CT numbers of the individual iodine solutions averaged over all the five channels of that solution's concentration in the phantom, for all four measurements. The image noise was also averaged over several areas. The higher image noise in the 33.25 keV image, compared to the 43 keV image, is attributed to smaller x-ray transmission (1/75 for 33.25 keV against 1/36 for 43 keV in the 13.5 cm acrylic phantom), which resulted in larger, uncorrected detector nonlinearities. The CT numbers for the 240 μg I ml^{-1} channels are 26 ± 3, 18 ± 1, 13 ± 3, and 9 ± 3 HU for 33.25 and 43 keV MECT and 80 and 100 kVp CCT, respectively. The corresponding numbers from the simulations are 26 ± 1.5, 17 ± 1.2, 12 ± 2.6, and 9 ± 1.9 HU, respectively (table 5). These results indicate a twofold to threefold advantage in iodine image contrast for MECT over CCT at beam energies relevant in imaging the human neck.

We note that the reason the iodine channels look darker than the phantom's bulk in figures 8 (43 keV) and 10 (55 keV mean energy) but lighter in figure 9 (33 keV) is that

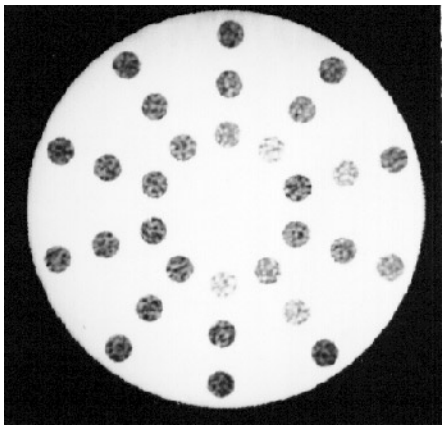

Figure 10. The iodine phantom imaged with CCT at 100 kVp.

at 43 and 55 keV the linear attenuation coefficient of acrylic is higher than that of water, while at 33 keV it is lower. At all energies, higher iodine concentrations are lighter in the image.

The iodine signal and noise results in figure 11 and table 5 can be used to estimate the minimum detectable iodine concentrations for each of the three measurements. However, comparison of the outcomes among the three is not valid because these measurements are not matched by their dose and spatial resolutions. Using the Rose condition (Rose 1948), indicating that the detectable signal must have a signal-to-noise ratio, SNR$\geqslant k$, where k ranges from three to seven, and assuming $k = 5$, we can deduce the minimum detectable iodine concentrations from the plots of figure 11. For example, the 43 keV MECT measurement has a noise of 1 HU, and, therefore, a detectable signal of 5 HU, which corresponds to a concentration of $\approx$ 100 mg I ml^{-1}. The corresponding iodine concentrations for the 33.25 keV MECT and 80 and 100 kVp CCT measurements are $\approx$ 150, $\approx$ 265, and $\approx$ 400 μg I ml^{-1}, respectively. The appearance of the CT images (figures 8–10) supports these results: successive channels are distinguished from each other mostly up to channels 3 or 4 in the 43 and 33.25 keV MECT images, and mostly up to channels 2 or 3 for the 100 kVp CCT image.

7. Summary and conclusions

Comparisons of image noise between the MECT and the CCT measurements are not conclusive because the parameters of the two systems were not matched. Such a matching is virtually impossible for two systems as different as MECT and CCT. Difficulties are accentuated by the strong dependence of noise on the shape of the MTF curve and on individual parameters affecting that shape, including the detector's resolution, source size, slice height, scan geometry, image pixel size, reconstruction geometry and reconstruction filter, and possibly other post-reconstruction filtration features. However, we can suggest that MECT has an advantage in having lower noise than CCT; the simulation results are a testimony to this point. The results on iodine contrast are conclusive: MECT immediately above the iodine K-edge has a twofold to threefold advantage over CCT depending on beam energies used for MECT and CCT. This advantage of MECT may be significant for CT angiography of the neck.

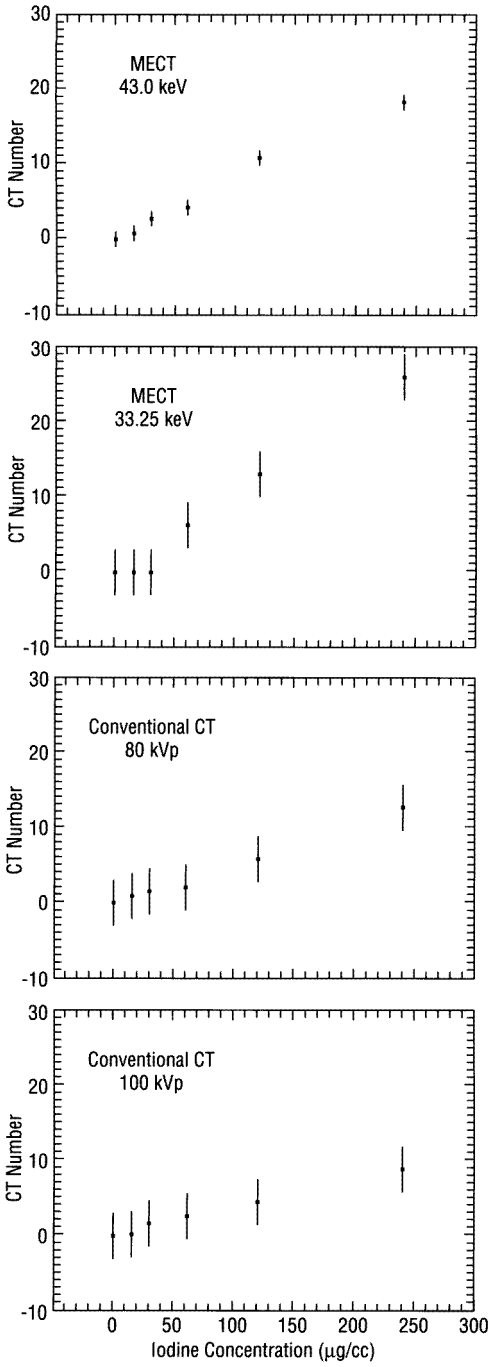

Figure 11. The CT numbers in iodine channels for the MECT and CCT images.

The MECT results were hampered by the instability of the beam's profile, the large pitch of the low-resolution detector that required its extensive masking, and the lack of correction

routines for the detector's non-linearity. These limitations will be removed: a bent Laue–Laue monochromator (Schulze *et al* 1994) using Si⟨331⟩ crystals is being constructed to alleviate the problem of beam-profile instability; a new detector with 0.9 mm element pitch is being developed; and non-linearity correction software is being installed.

Acknowledgments

We thank the following for their help: E F Becker, J M Dobbs, M H Miller, and H Weedon (Analogic Corp., Peabody, MA); L Perna (Bicron, Solon, OH), L E Berman, J F Gatz, N F Gmür, J B Hastings, X Huang, D D Joel, M Kershaw, A Lenhard, E McKenna, R Menk, P L Micca, M M Nawrocky, M Radulescu, D P Siddons, G C Smith, F A Staicu, G M Van derLaske, and M H Woodle (BNL); J Arenson and E Dafni (Elscint, Haifa); and G Gindi, A M Indelicato, C Mazzarese, R T Shults, and P Stephens (SUNY at Stony Brook). Comments of J S Gatley, R B Setlow, and A D Woodhead (BNL), and the technical assistance of A L Ruggiero (BNL), are also appreciated. This research has been supported by the Office of Health and Environmental Research of the United States Department of Energy.

References

Arenson J 1995 Data collection strategies: gantries and detectors *Medical CT and Ultrasound: Current Technology and Applications* ed L W Goldman and J B Fowlkers (College Park, NY: American Association of Physicists in Medicine) pp 329–48

Cann C E and Genant H K 1980 Precise measurement of vertebral mineral content using computed tomography *J. Comput. Assist. Tomogr.* **4** 493–500

Dilmanian F A 1992 Computed tomography with monochromatic x rays *Am. J. Physiol. Imaging* **3/4** 175–93

Dilmanian F A, Garrett R F, Thomlinson W C, Berman L E, Chapman L D, Hastings J B, Luke P N, Oversluizen T, Siddons D P, Slatkin D N, Stojanoff V, Thompson A C, Volkow N D and Zeman H D 1991 Computed tomography with monochromatic x rays from the National Synchrotron Light Source *Nucl. Instrum. Methods* B **56/57** 1208–13

Goodsitt M M, Hoover P, Veldee M S and Hsueh SL 1994 The composition of bone marrow for a dual-energy quantitative computed tomography technique. A cadaver and computer simulation study *Invest. Radiol.* **29** 695–704

Grodzins L 1983a Optimum energies for x-ray transmission tomography of small samples *Nucl. Instrum. Methods* **206** 541–5

——1983b Critical absorption tomography of small samples *Nucl. Instrum. Methods* **206** 547–52

Hamberg L M, Kristjansen P E, Hunter G J, Wolf G L and Jain R K 1994 Spatial heterogeneity in tumor perfusion measured with functional computed tomography at 0.05 microliter resolution *Cancer Res.* **54** 6032–6

Joseph P M 1981 Artifacts in computed tomography *Technical Aspects of Computed Tomography Radiology of the Skull and Brain 5)* ed T H Newton and D G Potts (St Louis, MO: Mosby) ch 114, pp 3956–92

Kalender W A 1995 Principles and performance of spiral CT. *Medical CT and Ultrasound: Current Technology and Applications* eds L W Goldman and J B Fowlkers (College Park, NY: American Association of Physicists in Medicine College Park, NY) pp 379–410

Kress J 1995 Image reconstruction and processing in the MECT project *MA Thesis* Department of Physics, State University of New York at Stony Brook

McCollough C H 1995 Principles and performance of electron beam CT *Medical CT and Ultrasound: Current Technology and Applications* eds L W Goldman and J B Fowlkers (College Park, NY: American Association of Physicists in Medicine) pp 411–36

Nachaliel E *et al* 1992 Monochromatic computed tomography of the human brain using synchrotron X rays: technical feasibility *Nucl. Instrum. Methods* A **319** 305–10

Nickoloff E L and Riley R 1985 A simplified approach for modulation transfer function determinations in computed tomography *Med. Phys.* **12** 437–42

Rose A 1948 The sensitivity performance of the human eye on an absolute scale *J. Opt. Soc. Am.* **38** 196–208

Rubenstein E, Hofstadter R, Zeman H D, Thompson A C, Otis J N, Brown G S, Giacomini J C, Gordon H J, Kernoff R S, Harrison D C and Thomlinson W C 1986 Transvenous coronary angiography in humans using synchrotron radiation *Proc. Natl Acad. Sci. USA* **83** 9724–8

Rubin G D, Dake M D, Napel S A, McDonnel C H and Jeffrey R B Jr 1993 Three-dimensional spiral CT angiography of the abdomen: initial clinical experience *Radiology* **186** 147–52

Schulze C, Suortti P and Chapman D 1994 Test of a bent Laue double crystal fixed exit monochromator *Synchrotron Radiat. News* **3** 8–11

Seeger J M, Barratt E, Lawson G A and Klingman N 1995 The relationship between carotid plaque composition, plaque morphology, and neurologic symptoms *J. Surg. Res.* **58** 330–6

Shleifer M, Dilmanian F A, Staicu F A, and Woodle M H 1994 Mechanical design of a high-resolution tunable crystal monochromator for the multiple energy computed tomography project *Nucl. Instrum. Methods* A **347** 356–9

Spanne P 1989 X-ray energy optimization in computed microtomography *Phys. Med. Biol.* **34** 679–90

Stonestrom J P, Alvarez R E and Macovski A 1981 A framework for spectral artifact corrections in x-ray CT *IEEE Trans. Biomed. Eng.* **28** 128–41

Takeda T, Itai Y, Hayashi K, Nagata Y, Yamaji H and Hyodo K 1994 High Spatial Resolution CT with a synchrotron radiation system *J. Comput. Assist. Tomogr.* **18** 98–101

Thomlinson W, Chapman D, Gmür N and Lazarz N 1988 The superconducting wiggler beamport at the National Synchrotron Light Source *Nucl. Instrum. Methods* A **266** 226–33

Thompson A C, Llacer J, Campbell Finman L, Hughes E B, Otis J N, Wilson S and Zeman H D 1984 Computed tomography using synchrotron radiation *Nucl. Instrum. Methods* **222** 319–23

van Steenbergen A and NSLS staff 1980 The National Synchrotron Light Source, basic design and project status *Nucl. Instrum. Methods* **172** 25–32

Wu X-Y, Dilmanian F A, Chen Z, Ren B, Slatkin D N, Chapman D, Shleifer M, Staicu F A and Thomlinson W 1995 Multiple energy computed tomography (MECT) at the NSLS: status report *Rev. Sci. Instrum.* **66** 1346–7

Zeman H D and Siddons D P 1990 Contrast agent choice for transvenous coronary angiography *Nucl. Instrum. Methods* A **291** 67–73